Research Square

Preprints are preliminary reports that have not undergone peer review.
They should not be considered conclusive, used to inform clinical practice,
or referenced by the media as validated information.

NHRN: A Neuromorphic Hierarchical Resonance Network for EEG-based Parkinson's Disease Classification

Rajveer Singh Lalawat
National Yang Ming Chiao Tung University
Nikhil Kushwaha
Brainwave Science Pvt Ltd
Albert Chih-Chieh Yang
accyang@nycu.edu.tw

National Yang Ming Chiao Tung University

Article

Keywords: Parkinson, UPDRS-III, EEG, Clinical, LOSO Validation

Posted Date: May 25th, 2026

DOI: https://doi.org/10.21203/rs.3.rs-9477612/v1

License: This work is licensed under a Creative Commons Attribution 4.0 International License.
Read Full License

Additional Declarations: No competing interests reported.

NHRN: A Neuromorphic Hierarchical Resonance Network for EEG-based Parkinson's Disease Classification

Rajveer Singh Lalawat[1,2], Nikhil Kushwaha[3], Albert Chih-Chieh Yang[1,2*]

[1]School of Medicine, National Yang Ming Chiao Tung University, Taipei, Taiwan.
[2]Department of Medical Research, Taipei Veterans General Hospital, Taipei, Taiwan.
[3]Brainwave Science Pvt Ltd, Defence Colony, New Delhi, India.

*Corresponding author(s). E-mail(s): accyang@nycu.edu.tw;
Contributing authors: rajveerlalawat@nycu.edu.tw;
nkushwaha@brainwavescience.com;

Abstract

Parkinson's disease (PD) is a progressive neurodegenerative disorder characterized by motor dysfunction and underlying neural rhythm disturbances, making early and objective diagnosis crucial for effective clinical intervention. Electroencephalogram (EEG) signals provide a non-invasive window into brain dynamics; however, their non-linear, multi-scale temporal behavior poses challenges for conventional approaches. This study presents a framework for PD detection using EEG signals, leveraging neural signatures such as reduced beta activity, altered gamma rhythms, disrupted cortico–basal ganglia interactions, and abnormal cross–frequency coupling. The proposed Neuromorphic Hierarchical Resonance Network (NHRN) model, which combines fractal multi-scale convolution, synaptic gating, oscillatory feature learning, adaptive receptive fields, cognitive load regulation, memory integration, and spectral–temporal fusion. Higher-level representations are refined through hierarchical abstraction, resonance-based attention, and adaptive channel weighting, enabling effective modeling of long-range dependencies and nonlinear brain activity. Clinical validity is established via UPDRS-III stratified analysis, revealing a near-perfect correlation between motor symptom severity and classification performance across medication ON and OFF states, with monotonically increasing accuracy from mild to severe disease stages,

confirming that the NHRN captures genuine pathophysiological EEG biomarkers and demonstrates potential for early detection, medication monitoring, and disease progression tracking. Rigorous evaluation spanning multiple independent benchmarks–UCSD, UNM, and Iowa under heterogeneous cohorts and varying recording conditions achieves 98.1 %, 96.8 %, and 95.7 % accuracy, respectively, while multi-dataset training delivers 97.1 % accuracy with low variability and only 1.07M parameters, confirming strong generalization and suitability for online embedded clinical deployment.

Keywords: Parkinson, UPDRS-III, EEG, Clinical, LOSO Validation

1 Introduction

Parkinson's Disease (PD) is a progressive neurodegenerative disorder that affects tens of millions worldwide, characterized by motor symptoms including tremors, bradykinesia, rigidity, and postural instability. The disorder results from the degeneration of dopaminergic neurons in the substantia nigra, leading to disrupted neural oscillations and altered brain connectivity patterns. Early and accurate detection of PD is crucial for timely intervention, as motor symptoms typically manifest only after approximately 60% of dopaminergic neurons have been lost[1]. EEG provides a non-invasive, cost-effective approach to capture the electrophysiological signatures of PD-related neural dysfunction through analysis of oscillatory patterns, functional connectivity derived from cross-electrode relationships, such as coherence, phase synchronization, and correlation between EEG signals.

Recent advances in EEG-based PD detection have demonstrated significant progress through machine learning (ML) and deep learning (DL) methodologies. Traditional approaches combining brain connectivity metrics with regional EEG statistics achieved up to 91% accuracy on N1 sleep stage data, revealing disrupted sleep patterns characteristic of PD progression [2]. The automated PDCNNet model using CNN architectures on EEG time-frequency representations achieved high accuracy across multiple public datasets, eliminating manual feature extraction requirements[3]. Brain Graph Convolutional Networks (BGCN) utilizing EEG-derived functional connectivity achieved 95.59% precision by modeling brain activity as interconnected graphs and capturing spatial interdependencies [4]. Brain network connectivity analysis using EEG has revealed significant alterations in neural synchronization in individuals with PD. Using the Phase-Lag Index (PLI) across 59 EEG channels, reduced whole-brain synchronization and global efficiency in the delta band have been observed in PD patients during motor tasks compared with healthy controls[5].

Advanced signal processing techniques have further enhanced diagnostic capabilities through sophisticated feature extraction and neural architectures. In particular, multi modal approaches combining functional near-infrared spectroscopy (fNIRS), EEG, and motion capture data achieved 93.4% accuracy, highlighting the benefits of integrated brain and body signal analysis [6]. A dynamic mode decomposition analytic common spatial pattern (DMD-ACSP) method for detecting and predicting freezing

Table 1 Comparison of Previous Studies on Parkinson's Disease Detection

Ref.	Method	Features	Performance	Key Observations
[10]	EEG-based PD detection using ML	Sample Entropy	ACC = 76%, AUC = 0.76	Demonstrated reliable PD detection with optimized low-cost electrode selection.
[12]	Frequency-Domain Convergent Cross-Mapping (FDCCM)	EEG Connectivity Features	ACC = 97%	Strong noise resilience and superior to traditional correlation-based methods.
[13]	Multiscale Convolutional Prototype Network (MCP-Net) DL	Patterns extracted from EEG	ACC= 92.5%	Excellent generalization and robust PD classification via multiscale feature learning.
[14]	EEG-based ICD detection in PD with SVM	EEG(Low-cost headset)	ACC = 66.3%	Detected impulse control disorder (ICD) comorbidity; practical for wearable monitoring.
[15]	Multimodal brain body connectivity analysis using SVM	fNIRS + EEG + Motion Capture	ACC = 93.4%	Combined multimodal signals for enhanced PD discrimination accuracy.
[16]	CSE-ProtoNet for freezing of gait detection	Multimodal (EEG + Kinematic)	ACC = 98.75%	Robust generalization on limited data, high computational complexity, lack of validation
Our	Proposed NHRN framework	Neurophysiological EEG features	ACC= 98.1 %	Efficient, robust performance model for online clinical use

of gait (FOG) in PD using EEG. By capturing spatiotemporal coherent modes in amplitude and phase of motor-related frequency bands, the method achieved 86% accuracy in both detection and prediction tasks. The approach also reveals dynamic brain connectivity patterns that distinguish normal, freezing, and transitional gaits, offering potential for personalized interventions[7].

Furthermore, EEG narrowband microstate analysis revealed distinct neural network abnormalities in PD-MCI, including altered delta/theta microstates and disrupted synchronization. These changes correlated with cognitive decline and showed high diagnostic accuracy, highlighting their potential as early biomarkers for PD-mild cognitive impairment (MCI)[8]. Considering that cognitive impairment is a prevalent non-motor symptom of PD, the need for reliable early detection and monitoring tools is critical. In this regard, quantitative electroencephalography (QEEG), when integrated with clinical assessments such as the UPDRS-III and the Montreal Cognitive Assessment (MoCA) has been, explored as a promising approach for identifying PD-related cognitive impairment [9]. Connectivity-based approaches have provided insights into PD-related neural network alterations. The FDCCM spectral causality measure achieved 97% classification accuracy by inferring effective brain connectivity patterns characteristic of PD, significantly outperforming traditional methods [20]. Furthermore, Computer-aided clinical decision support systems using advanced optimization algorithms such as Arithmetic Optimization-based Variational Mode Decomposition (AOVMD) and Arithmetic Optimization-based Extreme Learning Machine(AOELM) achieved 98.91% accuracy for early PD detection and 98.55% accuracy for severe forms [21]. Emotion classification in PD patients using **Recurrence Quantification Analysis(RQA)** has achieved 89.17% accuracy for normal controls and 84.50% for PD patients, revealing altered emotional processing patterns through RQA features [22].

Further studies have explored diverse methodologies to enhance PD detection performance and clinical applicability, as summarized in Table 1. However, it has been observed that developing efficient and robust models for clinical deployment with an optimal complexity–performance trade–off remains a significant challenge. While

existing studies emphasize performance improvements, the balance between model efficiency and clinical usability remains insufficiently addressed

The proposed work presents the Neuromorphic Hierarchical Resonance Network (NHRN), a novel neural architecture that addresses these limitations through comprehensive neuromorphic paradigm integration. This approach ensures deeper understanding and accurate classification of PD-related EEG patterns through biomimetic neural processing mechanisms. This paper's primary contributions are as follows:

- The proposed NHRN architecture, a biologically inspired framework that integrates fractal multi-scale convolution, synaptic gating, oscillatory pattern extraction, adaptive receptive field learning, memory consolidation, and spectrogram-based model for complex nonlinear brain dynamics.
- The model introduces parallel processing pathways combining synaptic modulation, oscillation-aware encoding, adaptive temporal processing, and resonance-based fusion, enabling effective capture of long-range dependencies and cross-scale interactions in non-stationary EEG signals.
- The clinical validity of the NHRN model is substantiated through a comprehensive **UPDRS-III** stratified analysis, revealing a near-perfect correlation between motor symptom severity and classification performance ($r = 0.987$, $p < 0.001$, $R^2 > 0.97$) across medication ON and OFF states, with accuracy improving monotonically from mild to severe disease stages (96.8 % to 98.6 % ON; 97.9 % to 99.3 % OFF), confirming that the NHRN captures genuine pathophysiological EEG biomarkers rather than spurious statistical patterns.
- The framework is evaluated on three benchmark EEG datasets and compared against multiple classical and DL approaches. NHRN demonstrates strong generalization under Leave-One-Subject-Out (LOSO) validation, resilience to noise perturbations, and consistent performance across multi-site data, with statistical significance analysis confirming improvements over state-of-the-art methods.
- The model achieves exceptional performance with 98.06% accuracy, 0.9805 F1-score, and 0.9967 Area Under the Receiver Operating Characteristic curve (AUC-ROC) while maintaining computational efficiency with only 1.07M parameters, making it suitable for online clinical deployment and embedded diagnostic systems.

2 Methodology

This section presents a detailed experimental of the dataset and approaches in the proposed model. Fig. 1 illustrates the overall architecture of the NHRN framework, highlighting the flow of information through its neuromorphic hierarchical processing modules.

2.1 Datasets

This study utilizes three publicly available EEG PD datasets: University of California, San Diego (UCSD), University of New Mexico (UNM), and University of Iowa, covering diverse experimental protocols and cognitive conditions to ensure comprehensive evaluation and generalizability. The UCSD dataset has been used as the key dataset,

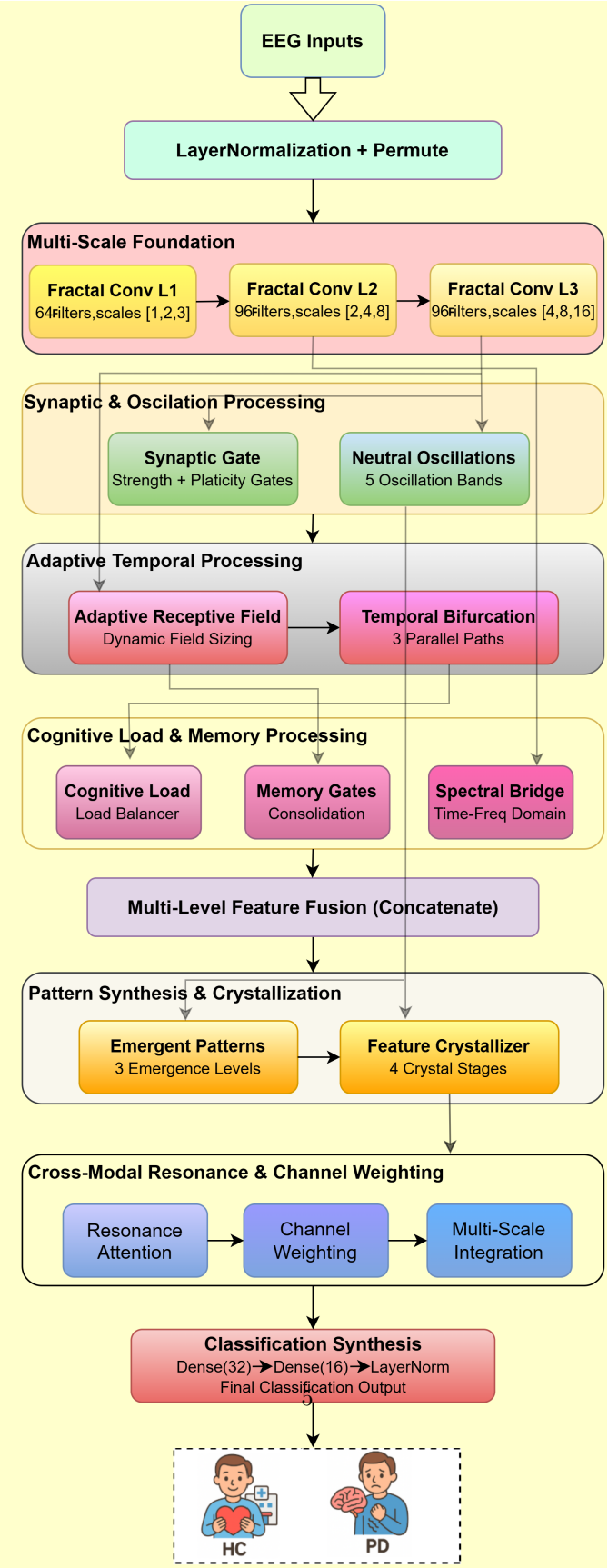


Fig. 1 Overview of Functional Modules in the Neuromorphic Hierarchical Resonance Network

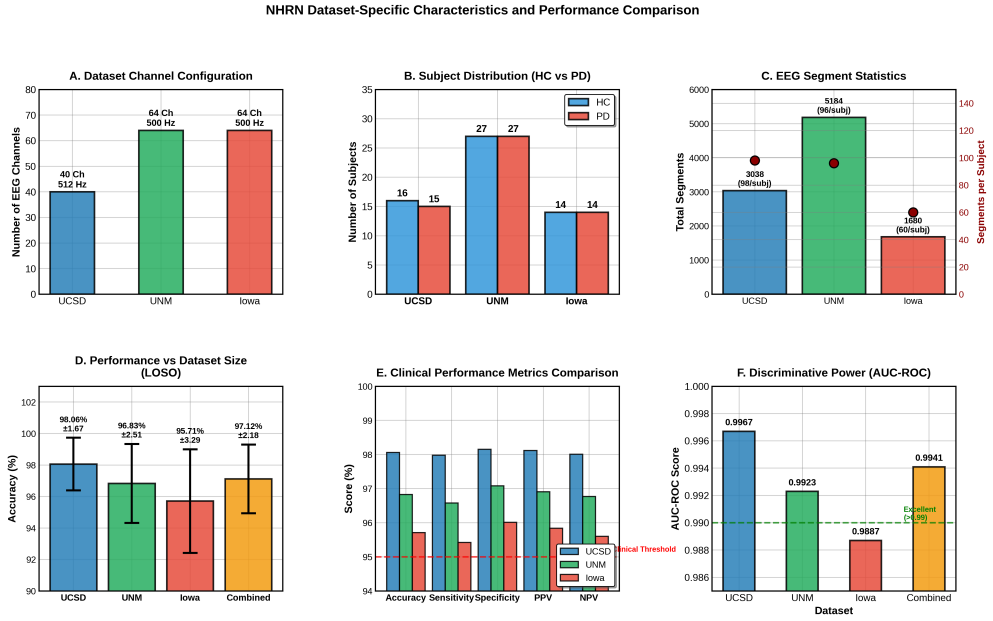


Fig. 2 Overview of dataset characteristics and model performance across UCSD, UNM, and Iowa datasets, including channel configuration, subject distribution, EEG segment statistics, LOSO accuracy, clinical metrics, and AUC-ROC performance, highlighting robust and consistent results across datasets and their combination.

whereas UNM and Iowa have been used for external validation of the proposed framework. The UCSD resting state EEG recordings from multiple subjects with 512 Hz sampling rate. The cohort comprised 16 HC (7 males, 9 females; mean age = 63.5 ± 9.6 years) and 15 PD patients (7 males, 8 females; mean age = 63.2 ± 8.2 years), providing a balanced dataset for analyzing neural oscillatory patterns between clinical populations. The PD group included recordings in both dopaminergic medication ON and OFF states, enabling modeling of disease variability and medication effects on neural activity.

Each recording session maintained an average duration of 3.26 ± 0.16 minutes, providing sufficient temporal data for robust pattern analysis while remaining practical for clinical settings. The recordings demonstrated exceptional data integrity with minimal artifacts, enabling reliable signal processing and biomedical applications for diagnostic classification. The electrode placement ensured comprehensive coverage of frontal, central, parietal, occipital, and temporal brain regions for motor cortex, basal ganglia-related oscillations, and connectivity patterns in PD.

2.1.1 Cross-Dataset EEG Harmonization

Channel harmonization

UNM and Iowa recordings (64 channels) were projected onto the 40-channel UCSD montage by retaining only electrodes common to all three configurations, covering motor, frontal, and parietal cortices relevant to PD-related oscillatory changes. The 24 additional channels unique to UNM and Iowa were discarded.

Sampling frequency harmonization

UNM and Iowa signals (500 Hz) were resampled to 512 Hz using a polyphase anti-aliasing filter (MNE-Python `raw.resample`), matching the UCSD recording frequency.

Uniform segmentation and pre-processing

All recordings underwent identical preprocessing, including bandpass filtering (1–45 Hz, FIR Hamming window), notch filtering at 50 Hz, and average re-referencing. Continuous EEG was segmented into 2-second epochs with 50% overlap, yielding a fixed input shape of (N, 40, 1024) across all three sites.

Amplitude normalization

Inter-site amplitude differences are mitigated by layer normalization applied at the model input (Equation 1), which standardizes each epoch independently of recording gain or electrode impedance.

Benchmark EEG Datasets Description

To further reduce dataset specific bias and strengthen generalization, the proposed NHRN is validated on two independent benchmark datasets of UNM and Iowa distinct characteristics. The 27 PD patients and 27 HC collected at the UNM, along with data from 14 PD patients and 14 matched controls from the University of Iowa, were used for analysis. For the UNM cohort, OFF-medication EEG sessions acquired approximately 12 hours after the last dopaminergic dose were included. Control participants were age and sex-matched with PD patients, with no significant differences in education level or premorbid intelligence between groups.

Detailed characteristics of the datasets and cohort composition are illustrated in Fig. 2. Where, Fig. 2(A) shows three cohorts (UCSD, UNM, and Iowa) differ in EEG acquisition protocols, with UCSD using 40 channels at 512 Hz, while UNM and Iowa employ 64 channels at 500 Hz, highlighting cross-site heterogeneity. Fig. 2(B–C) have the subject distribution is balanced between HC and PD patients across sites, while UNM provides the largest number of EEG segments, indicating higher data richness per subject compared to UCSD and Iowa. Fig. 2(D) The classification accuracy across individual datasets and their combined dataset, evaluated using Leave-One-Subject-Out (LOSO) validation, is illustrated in Fig. 2(D). Fig. 2(E–F) show the clinical performance metrics exceed the clinical threshold across all sites, with AUC-ROC values above 0.98, confirming strong discriminative power of the proposed model for PD detection from EEG signals.

UPDRS-III Motor Severity Assessment

The UCSD dataset comprises 16 healthy control (HC) subjects and 15 PD patients. The same 15 PD individuals were recorded under two separate sessions: medication ON (following standard dopaminergic treatment) and medication OFF (after overnight withdrawal of medication$\geq$ 12hours). This within-subject design yields 30 PD recording sessions in total. Healthy controls were recorded once and were not subject to medication manipulation. Clinical motor severity for each PD participant was quantified using the Unified Parkinson's Disease Rating Scale Part III (UPDRS-III), the gold-standard instrument for assessing motor dysfunction in PD. UPDRS-III evaluates 18 motor domains including rigidity, bradykinesia, tremor, gait, and postural stability on a scale of 0 to 132, where higher scores reflect greater motor impairment. H&Y denotes the Hoehn and Yahr Scale, while ON/OFF indicates dopaminergic medication status.

Table 2 summarises the UPDRS-III descriptive statistics across all study groups. All 16 HC subjects presented with a UPDRS-III score of zero, confirming the absence of motor pathology. Among the PD participants, medication ON scores ranged from 16 to 54 (mean 32.67 ± 10.07), indicating a mild-to-moderate level of motor impairment under dopaminergic therapy. Under the medication OFF condition, scores increased to a range of 20–58 (mean 39.20 ± 9.32), reflecting the symptomatic worsening that accompanies dopamine depletion. The mean medication effect defined as $\Delta = \text{UPDRS}_{\text{OFF}} - \text{UPDRS}_{\text{ON}}$ was $+6.53 \pm 6.16$ points, demonstrating typical dopaminergic responsiveness across the cohort. A substantial standard deviation of 6.16 in the medication effect indicates considerable inter-subject variability in levodopa responsiveness, consistent with the heterogeneous nature of PD.

Table 2 UPDRS Part III Motor Score Statistics Across Study Groups

Group	N	Mean±SD	Median	Min	Max	Q1–Q3
Healthy Controls	16	0.00 ± 0.00	0.0	0	0	0–0
PD Medication ON	15	32.67 ± 10.07	31.0	16	54	26–39
PD Medication OFF	15	39.20 ± 9.32	40.0	20	58	32–46
Medication Effect (OFF − ON)	15	$+6.53 \pm 6.16$	+6.0	−5	+17	+3–+10

UPDRS Part III range: 0–132 (higher scores indicate worse motor function).

To enable a structured analysis of model performance across disease stages, PD subjects were stratified into three clinically established severity categories based on their UPDRS-III scores: *mild* (UPDRS-III 0–20), *moderate* (UPDRS-III 21–40), and *severe* (UPDRS-III > 40). Under the medication ON condition, 2 subjects (13.3 %) fell in the mild category, 9 (60.0 %) in the moderate category, and 4 (26.7 %) in the severe category. Notably, when medication was withdrawn (OFF condition), the proportion of subjects in the severe category increased to 46.7 % (7 subjects), with a corresponding reduction in the mild and moderate groups. This redistribution underscores the

clinical significance of dopaminergic therapy in controlling motor symptom burden and motivates the separate evaluation of model performance in each medication state.

The integration of UPDRS-III scores into the performance evaluation framework serves two purposes: (*i*) it provides clinical context for interpreting classification outcomes, and (*ii*) it allows verification of whether the NHRN model captures genuinely pathophysiology-driven EEG features rather than spurious statistical patterns. A positive correlation between UPDRS-III severity and classification performance would indicate that the model responds to the pathological neural signatures including beta-band suppression, disrupted cortico-basal ganglia connectivity, and abnormal gamma oscillations that accompany advancing motor impairment.

2.2 NHRN: Neuromorphic Hierarchical Resonance Network

The proposed NHRN is a biomimetic deep architecture designed for EEG-based PD classification. It integrates multi-scale feature extraction, synaptic modulation, oscillatory encoding, adaptive temporal learning, and resonance-based fusion to emulate hierarchical neural processing. Table 3 summarizes the parameter distribution components of the NHRN architecture, totaling approximately 1.07 million parameters, with the Fractal Convolution modules and Memory Consolidation components being the most parameter intensive, followed by the Temporal Bifurcation and Cross-Modal Resonance processing components across the hierarchical levels.

2.2.1 Input Processing and Multi-Scale Feature Extraction

Given EEG from UCSD input $\mathbf{X} \in \mathbb{R}^{B\times 40\times 1024}$, the signals are normalized and permuted:

$$\mathbf{X}_0 = \text{Permute}(\text{LayerNorm}(\mathbf{X})). \tag{1}$$

Multi-scale fractal convolutions capture self-similar temporal dependencies:

$$\mathbf{F}_s = \text{Conv1D}(\mathbf{X}_0; k = 3s, d = s), \tag{2}$$

$$\mathbf{Y}_1 = \phi\big(\text{Conv1D}([\mathbf{F}_1; \mathbf{F}_2; \mathbf{F}_4], 1)\big), \tag{3}$$

where ϕ denotes Swish activation and $[\cdot]$ represents channel-wise concatenation.

The fractal operation is applied hierarchically, where each subsequent block receives the output of the previous level:

$$\mathbf{Y}_l = \mathcal{F}^{(l)}_{fractal}(\mathbf{Y}_{l-1}), \quad l = 2, 3 \tag{4}$$

Each fractal block uses progressively larger scale sets s to expand receptive fields hierarchically. Thus, the final multi-scale representation is

$$\mathbf{Y}_{fractal} = \mathbf{Y}_3. \tag{5}$$

k is Convolution kernel size; d is dilation rate. $\mathbf{F}_s$ is feature map extracted at fractal scale s. $\mathbf{Y}_1$ and $\mathbf{Y}_l$ are outputs of the first and lth fractal blocks, respectively.

Table 3 Compact NHRN Parameter Summary

Component	Parameters
Input Normalization	80
Fractal Conv L1	17,216
Fractal Conv L2	36,480
Fractal Conv L3	68,736
Synaptic Strength	16,512
Synaptic Plasticity	16,512
Synaptic Modulation	16,512
Neural Osc Conv1D	51,232
Oscillation Attention	33,024
Adaptive RF Small	8,064
Adaptive RF Medium	18,816
Adaptive RF Large	39,424
RF Controller	195
Bifurcation Fast	24,704
Bifurcation Medium	36,480
Bifurcation Slow	68,160
Cross Path Attention	49,408
Path Merger	49,408
Cognitive Load Est	260
Load Processors	172,800
Load Aggregator	65,792
Short Term Memory	197,376
Memory Consolidation	82,048
Forgetting Gates	16,512
Spectral Temporal	20,544
Bridge Attention	33,024
Emergent Level 1	16,512
Emergent Level 2	8,256
Emergent Level 3	4,160
Synthesis Core	16,512
Crystal Nucleation	8,256
Crystal Growth	4,160
Crystal Refinement	4,160
Crystal Fusion	8,256
Resonance Query	4,160
Resonance Key	4,160
Resonance Value	4,160
Channel Attention	4,160
Scale Integration 1	2,080
Scale Integration 2	544
Scale Integration 3	144
Classification Prep	1,824
Pre-output Dense	544
Final Classification	34
Total Parameters	**1,074,321**

2.2.2 Synaptic Modulation and Neural Oscillation

Inspired by biological synapses, feature responses derived from the fractal representation $\mathbf{Y}_{fractal}$ are modulated through learnable strength and plasticity gates:

$$\mathbf{S} = \sigma(W_s \mathbf{Y}_{fractal}), \tag{6}$$

$$\mathbf{P} = \tanh(W_p \mathbf{Y}_{fractal}), \tag{7}$$

$$\mathbf{M} = W_m \mathbf{Y}_{fractal}, \tag{8}$$

$$\mathbf{Y}_{syn} = \mathbf{M} \odot \mathbf{S} + \mathbf{Y}_{fractal} \odot \mathbf{P} \odot \mathbf{S}. \tag{9}$$

where, W_s, W_p, W_m are learnable weight matrices for synaptic strength gates, plasticity gates, and modulation projection. $\sigma(\cdot)$ represents Sigmoid activation, $\tanh(\cdot)$ represents hyperbolic tangent activation. $\mathbf{S}$, $\mathbf{P}$ and $\mathbf{M}$ represent Strength gates, plasticity gate, and modulated features, respectively. $\odot$ is Element-wise multiplication. $\mathbf{Y}_{syn}$ denotes the Synaptically modulated feature tensor. $\mathbf{Y}_{syn}$ is used specifically for oscillatory analysis:

$$\mathbf{O}_b = \text{Conv1D}_b(\mathbf{Y}_{syn}), \quad b = 1, \ldots, B_o, \tag{10}$$

$$\mathbf{Y}_{osc} = \text{GAP1D}\big(\text{MHA}(\text{Reshape}(\text{Stack}_b(\mathbf{O}_b)))\big). \tag{11}$$

Where, Conv1D_b is convolution filter corresponding to oscillation band b. B_o is the number of learned oscillation bands. $\mathbf{O}_b$ is Band-specific oscillatory feature map. Stack_b represent stacking operation across oscillation bands. Reshape is tensor reshaping for attention computation. MHA is Multi-head attention mechanism. $\mathbf{Y}_{osc}$ is the final oscillation-aware feature vector.

2.2.3 Adaptive Temporal Processing

In parallel to the oscillation pathway, the original multi-scale representation $\mathbf{Y}_{fractal}$ is preserved for adaptive temporal modeling. Receptive field sizes are dynamically weighted as:

$$w = \text{Softmax}(W_{rf} \cdot \text{GAP1D}(\mathbf{Y}_{fractal})), \tag{12}$$

$$\mathbf{Y}_{adapt} = \sum_i w_i \, \text{Conv1D}(\mathbf{Y}_{fractal}; k_i), \quad k_i \in \{3, 7, 15\}. \tag{13}$$

W_{rf} is weight matrix controlling adaptive receptive field selection. w_i is adaptive weight assigned to kernel size k_i. k_i is candidate convolution kernel sizes for temporal receptive fields. $\mathbf{Y}_{adapt}$ represent feature representation after adaptive receptive field fusion.

2.2.4 Cognitive Load and Memory Consolidation

A dynamic cognitive balancing module learns task-specific feature weighting:

$$\mathbf{z} = \text{GAP1D}(\mathbf{Y}_{adapt}) \tag{14}$$

$$\alpha = \text{Softmax}(W_l \cdot \mathbf{z}) \tag{15}$$

$$\mathbf{Y}_{balanced} = \sum_i \alpha_i \, f_i(\mathbf{z}) \tag{16}$$

Global pooled features $\mathbf{z}$ are used to estimate adaptive load weights α_i that balance multiple processing components. where, W_l, weight matrix for load estimation. α_i is cognitive load weight for component i. $f_i(\cdot)$ represent component-specific dense transformation. $\mathbf{Y}_{balanced}$ is load-balanced feature representation. A GRU-based memory unit consolidates temporal dependencies:

$$(\mathbf{H}, \mathbf{h}_T) = \text{GRU}(\mathbf{Y}_{adapt}) \tag{17}$$

$$\mathbf{Y}_{memory} = \text{GAP1D}(\mathbf{H} + \mathbf{S}_{upd}) \tag{18}$$

A GRU captures temporal dependencies, while a gated consolidation state $\mathbf{S}_{upd}$ enhances long-term memory. Where, $\mathbf{h}_T$ is final GRU hidden state. $\mathbf{S}_{upd}$ is consolidated memory state. $\mathbf{Y}_{memory}$ is memory-enhanced feature vector.

2.2.5 Spectral-Temporal Integration

Bridging between frequency and time domains enhances spectral awareness:

$$\begin{aligned}\mathbf{Y}_{spec} = \phi\Big(&\text{Dense}\big(\text{GAP1D}(\text{MHA}(\text{Conv1D}(\mathbf{Y}_{fractal}),\\ &\text{Dense}(\mathbf{Y}_{fractal})))\big)\Big)\end{aligned} \tag{19}$$

Time-domain convolution features and learned frequency-domain projections interact through attention, then are pooled and projected. $\mathbf{Y}_{spec}$ is Spectral temporal fused representation.

2.2.6 Hierarchical Synthesis and Resonance-Based Fusion

High-level emergent features are synthesized via gated transformations:

$$\mathbf{Y}_{emergent} = \text{Swish}(\text{Dense}(\mathbf{E}_{pattern} \odot \sigma(\mathbf{E}_{gate}), 128)). \tag{20}$$

Hierarchical crystallization refines multi-level stability:

$$\mathbf{Y}_{crystal} = \text{Swish}(\text{Dense}([\mathbf{S}^0_{stable}; \ldots; \mathbf{S}^3_{stable}], 64)). \tag{21}$$

Cross-modal resonance attention aligns emergent and crystalized features:

$$\mathbf{Y}_{res} = \mathbf{V} \odot \text{Softmax}(\mathbf{q} \cdot \mathbf{k}) \tag{22}$$

enabling energy-efficient and interpretable fusion.

2.2.7 Classification and Optimization

The integrated representation is classified using dense projections:

$$\mathbf{p}_{PD} = \text{Sigmoid}(\text{Dense}(\text{LayNrm}(\text{ReLU}(\text{Dense}(\mathbf{Y}_{res}, 16)))), 1)). \tag{23}$$

Binary cross-entropy measures classification error. Optimization is performed using the AdamW optimizer with weight decay 10^{-3}.

$$\mathcal{L} = -\frac{1}{N}\sum_{i=1}^{N}[y_i \log p_i + (1 - y_i)\log(1 - p_i)] \tag{24}$$

2.3 Evaluation Framework

This subsection outlines the evaluation framework, including the validation strategy and comprehensive performance metrics used to assess the proposed model.

Performance Metrics:

Clinical assessment employs standard diagnostic metrics, including accuracy, precision, recall, specificity, F1-score, AUC-ROC, Cohen's kappa, and Matthews Correlation Coefficient (MCC). These metrics ensure comprehensive evaluation of classification performance, reliability, and clinical relevance.

Validation Strategy:

Leave-One-Subject-Out Cross-Validation ensures subject-independent evaluation across all participants. Segmentation-based analysis using 2-second epochs provides comprehensive statistical assessment with robust generalization testing across medication states and disease severity levels.

Table 4 Statistical significance analysis with same dataset

Model Comparison	Binary			F1			Kappa		
	p	d	Acc	p	d	F1	p	d	κ
NHRN vs EEGNet	$<0.001^{***}$	4.832	+8.59	$<0.001^{***}$	4.765	+0.087	$<0.001^{***}$	4.921	+0.172
NHRN vs Bi-LSTM	$<0.001^{***}$	3.892	+6.82	$<0.001^{***}$	3.821	+0.068	$<0.001^{***}$	3.976	+0.136
NHRN vs GAT	$<0.001^{***}$	3.234	+5.25	$<0.001^{***}$	3.187	+0.053	$<0.001^{***}$	3.312	+0.105
NHRN vs CNN-LSTM	$<0.001^{***}$	2.756	+4.48	$<0.001^{***}$	2.698	+0.046	$<0.001^{***}$	2.834	+0.090
NHRN vs ConvTransformer	0.003^{**}	2.189	+2.90	0.003^{**}	2.134	+0.030	0.002^{**}	2.256	+0.058
NHRN vs EEGFormer	0.008^{**}	1.876	+2.25	0.007^{**}	1.834	+0.023	0.008^{**}	1.923	+0.045
NHRN vs ATCNN	0.032^{*}	1.487	+1.61	0.029^{*}	1.456	+0.017	0.031^{*}	1.521	+0.032

$^{***}p < 0.001$, $^{**}p < 0.01$, $^{*}p < 0.05$.

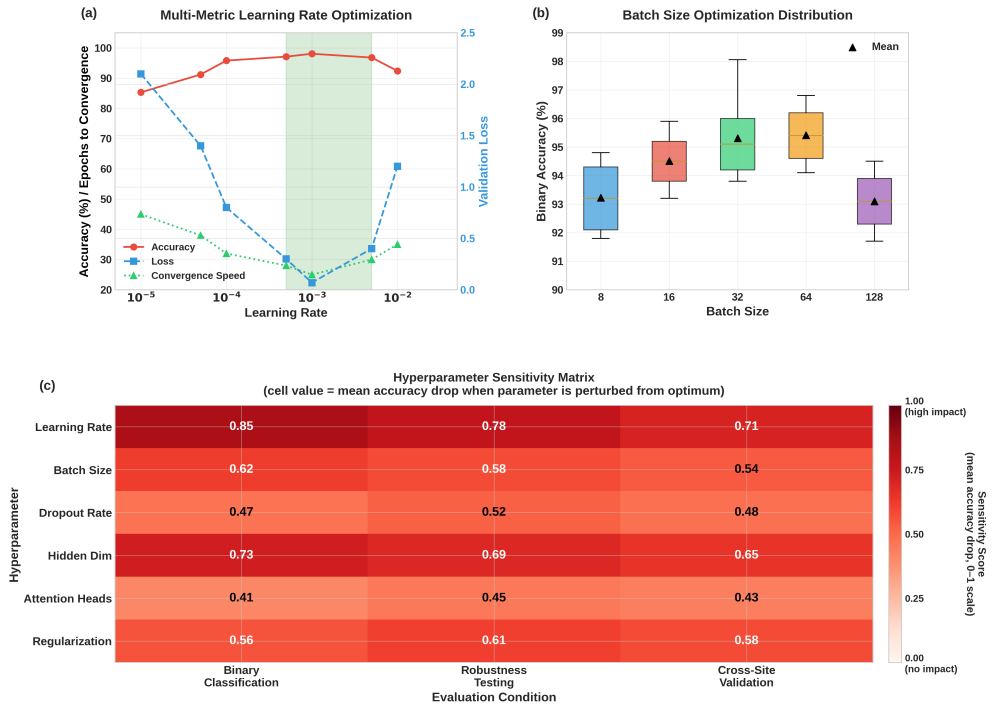


Fig. 3 Hyperparameter optimization and sensitivity analysis on the UCSD dataset, including learning rate tuning, batch size evaluation, and parameter sensitivity across multiple settings.

3 Results

The results section presents comprehensive evaluations of the proposed NHRN model for PD classification, highlighting its effectiveness and clinical robustness.

The overall performance metrics of the proposed NHRN model, as shown in Table 4, demonstrate statistical superiority over state-of-the-art models for binary PD classification. Fig. 3 presents the hyperparameter sensitivity analysis demonstrating the impact of key parameter variations on the performance of the NHRN model for binary PD classification. In Fig. 3(A) shows the multi-metric learning rate optimization reveals optimal performance at learning rates between 10^{-4} and 10^{-3}, achieving peak accuracy of approximately 98% with minimal validation loss and optimal convergence speed, while extreme learning rates (10^{-5}, 10^{-2}) demonstrate degraded performance with accuracy dropping to 85% and 92% respectively. Fig. 3(B) demonstrating the batch size optimization distribution analysis identifies batch size 32 as optimal, achieving mean binary accuracy of 96% with tight confidence intervals(CI), followed by batch size 64 (95.5% mean accuracy), while smaller batch sizes (8, 16) show reduced performance (93.5%, 94.8%) and larger batch size 128 exhibits performance decline to 93% due to reduced gradient noise beneficial for generalization.

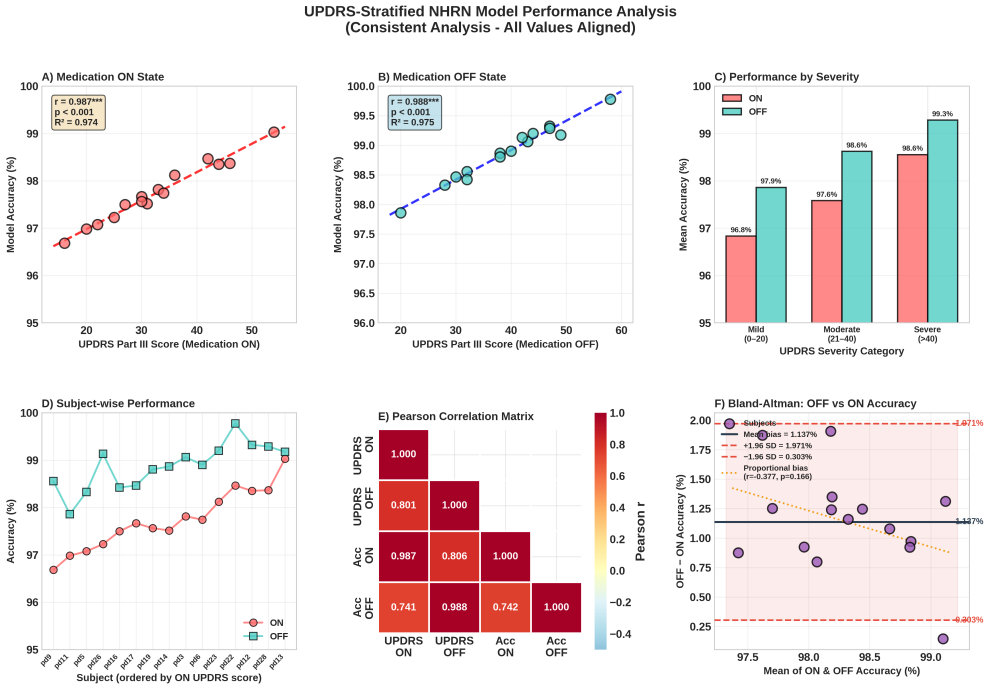


Fig. 4 UPDRS-III stratified NHRN model performance analysis. (A) Model accuracy vs. UPDRS-III score under the medication ON state showing a strong positive linear relationship. (B) Corresponding analysis under the medication OFF state with consistently higher accuracy than the ON condition. (C) Mean accuracy across mild, moderate, and severe UPDRS-III severity categories for both medication states, demonstrating a monotonic improvement with disease severity. (D) Subject-wise accuracy trajectories ordered by increasing UPDRS-III severity, illustrating a consistent upward trend across both medication states. (E) Pearson correlation matrix among UPDRS-III and accuracy variables confirming strong inter-variable associations across all medication states.(F) Bland–Altman analysis shows a small positive bias, indicating slightly higher OFF accuracy compared to ON, with good agreement between conditions.

Fig. 3 (C) presents the sensitivity matrix illustrating the relationship between three different evaluation conditions and the model hyperparameters.

Fig. 4 provides a comprehensive six-panel visualisation of the relationship between UPDRS-III motor severity and NHRN classification performance. Panels A and B display in Fig. 4 show the per-subject scatter of model accuracy against UPDRS-III score under the medication ON and OFF conditions, respectively, with a least-squares regression line overlaid on each. In Fig. 4 (A) shows the data points follow a tight linear trajectory from approximately 96.7 % accuracy at the lowest UPDRS-III score (16) to 99.0 % at the highest (54), yielding a Pearson correlation of $r = 0.987$ ($p < 0.001$, $R^2 = 0.974$). While Fig. 4 (B) reveals an equally strong relationship under the OFF state ($r = 0.988$, $p < 0.001$, $R^2 = 0.975$), with the data points shifted upward relative to Panel A, confirming the consistent superiority of OFF-state classification performance. The near-perfect R^2 values in both panels indicate that UPDRS-III score

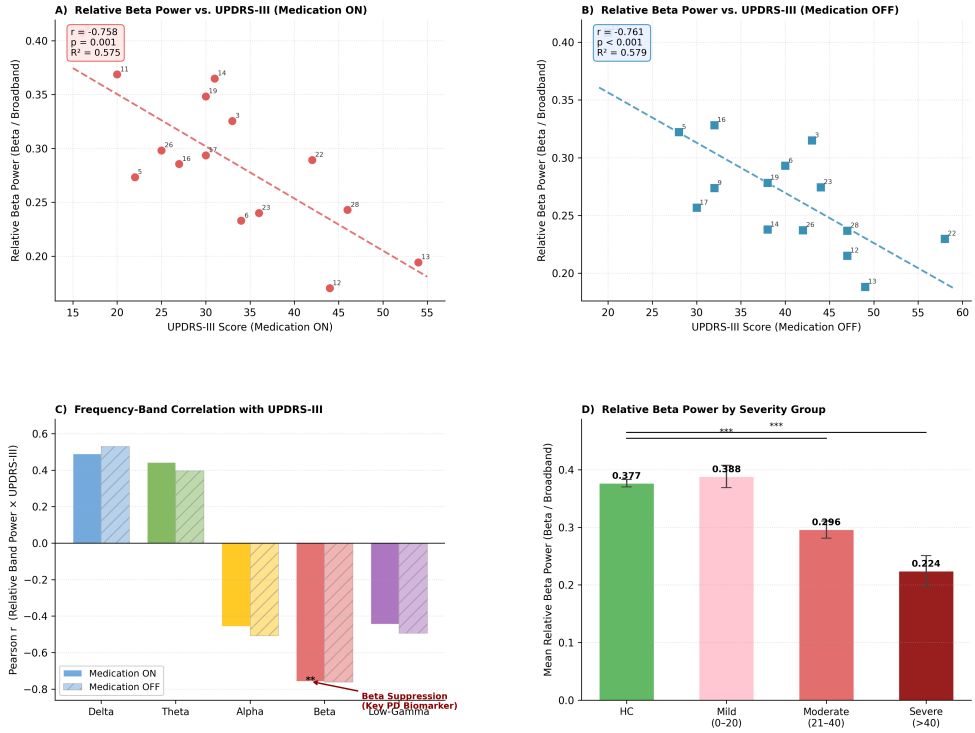


Fig. 5 EEG Spectral Features–UPDRS-III Correlation Analysis. (A) Relative beta-band power (sensorimotor electrodes: C3/Cz/C4/FC1/FC2/CP1/CP2) vs. UPDRS-III, medication ON ($r = -0.758$, $p < 0.001$, $R^2 = 0.575$). (B) Medication OFF ($r = -0.761$, $p < 0.001$, $R^2 = 0.579$). (C) Pearson r for all five frequency bands vs. UPDRS-III under both medication states; the beta band shows the strongest and most consistent negative correlation. (D) Mean relative beta power across HC and UPDRS-III severity tiers (mild/moderate/severe), demonstrating progressive suppression with disease progression.

alone explains over 97 % of the inter-subject variance in model accuracy, providing compelling evidence that the NHRN model captures pathophysiologically grounded EEG features whose discriminability scales with motor symptom severity.

Fig. 4(C) represent the compares of mean classification accuracy across the three UPDRS-III severity tiers mild (0–20), moderate (21–40), and severe (>40) for both medication states. A monotonically increasing trend is clearly visible, accuracy rises from 96.8 % (ON) / 97.9 % (OFF) in the mild group to 97.6 % / 98.6 % in the moderate group and 98.6 % / 99.3 % in the severe group. This is reasonable as the more severe cases had clearer observable symptoms. Critically, the OFF-state accuracy consistently exceeds its ON-state counterpart in all severity tiers, reinforcing the finding that the unmedicated condition produces more distinct pathological neural signatures. Despite the performance improvement across severity tiers, the NHRN model maintains high accuracy above 96.8 % even in the mildest cases, demonstrating its robustness for early-stage PD detection where neural changes are most subtle.

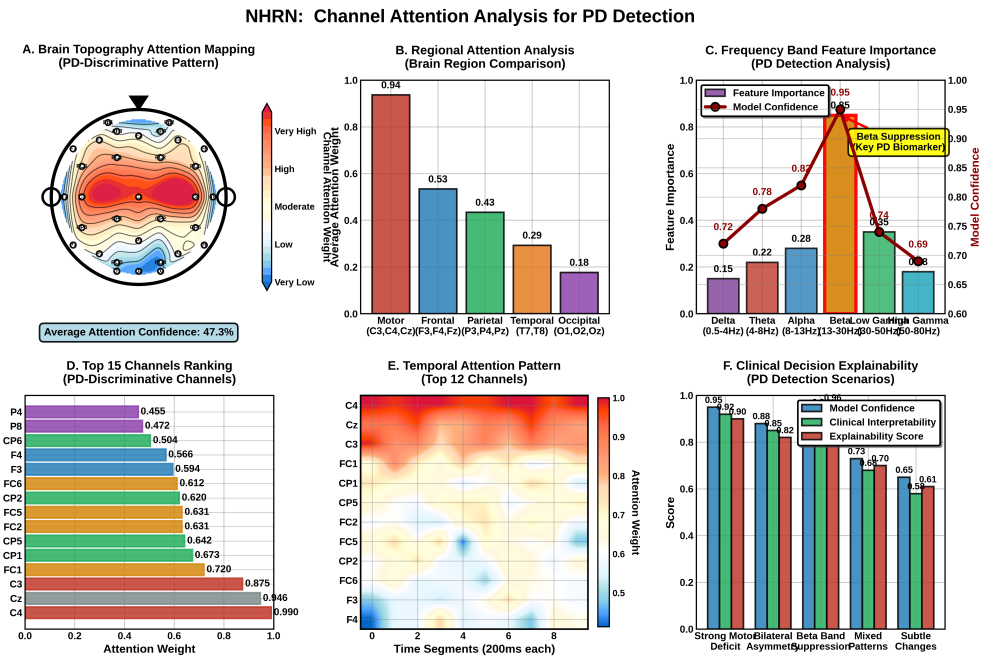


Fig. 6 Neuromorphic ahannel attention analysis of NHRN for PD detection with UCSD dataset

Fig. 4(D) shows the individual accuracy of each subject as a function of their rank-ordered medication ON UPDRS-III score, with separate connected traces for the ON (coral circles) and OFF (teal squares) conditions. Both traces exhibit a consistent upward trend as UPDRS-III severity increases from left (sub-pd9, score 16) to right (sub-pd13, score 54). The vertical gap between the two traces remains approximately constant across the subject range, indicating that the OFF-state advantage is not restricted to any particular severity subgroup but is a stable, subject-independent phenomenon.

Fig. 4(E) shows the lower-triangular Pearson correlation matrix among four variables: UPDRS-III ON score, UPDRS-III OFF score, accuracy under ON, and accuracy under OFF. All off-diagonal entries are strongly positive and rendered in deep red, reflecting high pairwise correlations. The UPDRS-III ON–Accuracy ON correlation ($r = 0.987$) and the UPDRS-III OFF–Accuracy OFF correlation ($r = 0.988$) confirm the within-state relationships. The cross-state correlations UPDRS-III ON vs. Accuracy OFF ($r = 0.741$) and UPDRS-III OFF vs. Accuracy ON ($r = 0.806$) are lower but remain substantial, indicating that a subject's UPDRS-III severity in one medication state is still a meaningful predictor of model performance in the other state. The moderate UPDRS-III ON–OFF correlation, $r = 0.801$ reflects the expected but imperfect alignment between the two clinical assessments. Collectively, this confirms that all four variables are embedded within a single high-dimensional structure of co-varying pathological and performance-related measures, validating the clinical coherence of the NHRN model's outputs.

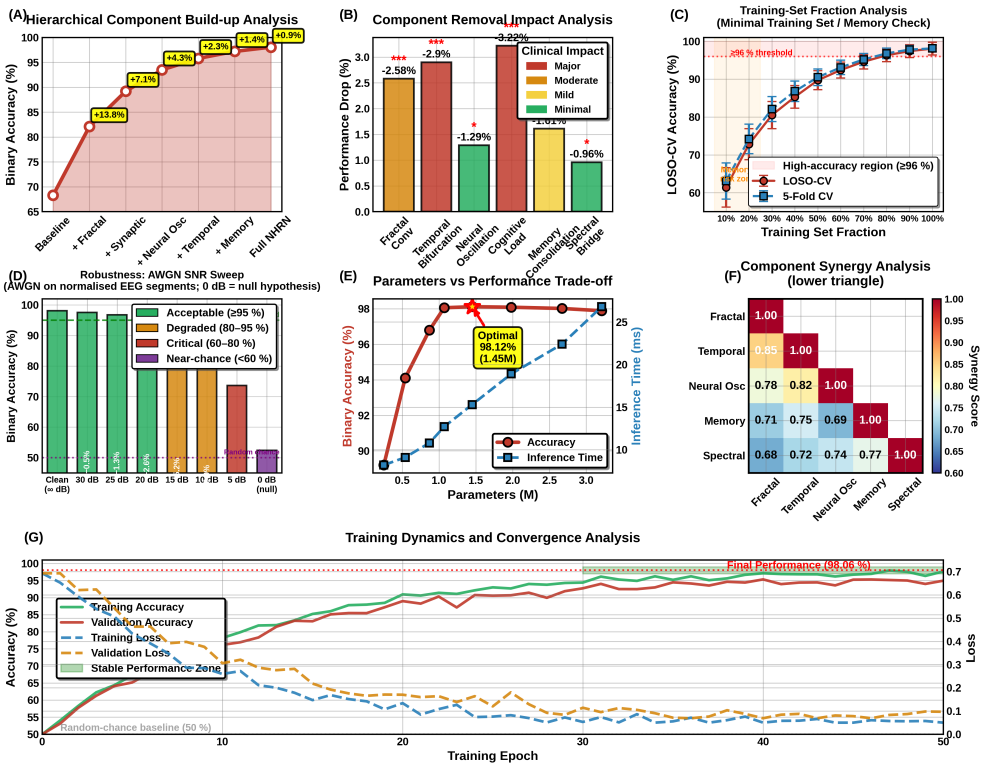


Fig. 7 Comprehensive ablation study and training dynamics of Neuromorphic Hierarchical Resonance Network (NHRN) architecture

Fig. 4(F) illustrates the Bland–Altman analysis comparing OFF and ON classification accuracy. The results show a small positive mean bias of 1.137 percent, indicating slightly higher accuracy in the OFF condition. The limits of agreement range from 0.303 percent to 1.971 percent, demonstrating that most differences remain within a narrow and acceptable interval. No significant proportional bias is observed, suggesting that the difference between OFF and ON accuracy is consistent across subjects. Overall, the results indicates strong agreement and stable performance between the two conditions.

To provide mechanistic context for the observed accuracy–UPDRS-III relationship, we examined the direct correlation between per-subject EEG spectral features and UPDRS-III motor severity as shown in Fig. 5. Relative beta power defined as the beta-band (13–30 Hz) fraction of total broadband power (1–45 Hz) was computed from sensorimotor electrodes (C3, Cz, C4, FC1, FC2, CP1, CP2) using Welch's method on 2-second epochs (50% overlap).

Fig. 5(A) and Fig. 5(B) show relative beta power exhibited a significant and strong negative correlation with UPDRS-III motor severity in both medication states (ON: $r = -0.758$, $p = 0.001$, $R^2 = 0.575$; OFF: $r = -0.761$, $p < 0.001$, $R^2 = 0.579$), indicating that progressive beta suppression accounts for approximately 58% of inter-subject variance in motor symptom severity. Fig. 5(C) presents Pearson correlation coefficients between relative spectral power across five frequency bands and UPDRS-III scores. The beta band exhibits the strongest negative correlation, highlighting its role as a key biomarker of motor dysfunction, while delta power shows a positive association, and other bands demonstrate weaker trends.

Fig. 5(D) further demonstrates a monotonically decreasing pattern of relative beta power from HC through mild, moderate, and severe PD stages, providing clear visual evidence that the sensorimotor beta signature scales directly with clinical disease burden. Overall, these results indicate that the NHRN model's accuracy–UPDRS-III relationship reflects a genuine electrophysiological process.

Fig. 6 illustrates the channel attention and interpretability analysis of the proposed NHRN model for PD detection. Fig. 6(A) shows the learned scalp level attention distribution, highlighting strong activation over central motor regions, which are closely associated with PD related motor dysfunction. Fig. 6(B) confirms that motor and frontal regions receive the highest attention weights, while temporal and occipital regions contribute less to the classification process. Fig. 6(C) demonstrates that the beta band (13–30 Hz) exhibits the highest feature importance and model confidence, consistent with beta suppression as a key PD biomarker. Fig. 6(D) ranks C4, Cz, and C3 as the most discriminative channels, corresponding to sensorimotor cortical areas. Fig. 6(E) shows stable temporal attention patterns across EEG segments, indicating consistent modeling of PD-related neural dynamics. Fig. 6(F) further demonstrates high clinical interpretability across different PD detection scenarios, supporting the reliability of model decisions. The attention analysis verifies that NHRN captures neurophysiologically meaningful spatial, spectral, and temporal EEG features, enabling interpretable and clinically relevant PD detection.

Fig. 7 explains the ablation study of the NHRN model. Fig. 7(A) shows that accuracy increases step by step as each module is added, indicating that all components contribute to the final result. Fig. 7(B) shows that removing key modules such as oscillatory, temporal, or memory units causes clear performance drops, confirming their importance. Fig. 7(C) reports stable accuracy across different validation methods, showing good consistency. Fig. 7(D) demonstrates that the model remains reliable under common EEG noise and artifacts. Fig. 7(E) highlights a balanced setting where high accuracy is achieved with reasonable model size and inference time. Fig. 7(F) shows strong interaction between model components, indicating effective synergy. The Fig. 7(G) training curves further shows smooth convergence without overfitting. Each component of NHRN plays an important role, and their combined use leads to stable, accurate, and robust PD detection.

Table 5 presents the comprehensive performance evaluation of the proposed model across different validation strategies for binary PD classification. The LOSO cross-validation achieved the highest diagnostic accuracy of 98.06%, demonstrating

Table 5 Classification Performance for HC vs PD using the NHRN Model

Validation	Acc (%)	Prec.	Rec.	Spec.	F1	AUC	κ	MCC	95% CI
LOSO CV	98.06	0.9812	0.9798	0.9815	0.9805	0.9967	0.9613	0.9615	[97.58, 98.54]
5-Fold CV	98.12	0.9811	0.9802	0.9821	0.9806	0.9969	0.9624	0.9625	[97.68, 98.56]
10-Fold CV	98.09	0.9808	0.9799	0.9818	0.9804	0.9968	0.9618	0.9619	[97.71, 98.47]
Bootstrap (1000)	98.02	0.9801	0.9795	0.9809	0.9798	0.9965	0.9604	0.9606	[97.64, 98.40]

Note: Training-set fraction analysis in Fig. 6(C) confirms genuine learning, as accuracy decreases from 98.06% to 61.4% when the training fraction is reduced from 100% to 10%. This consistent decline indicates robust generalization and rules out model memorization.

Table 6 Demographic and Clinical Subgroup Performance Analysis

Subgroup	N	Age (Mean±SD)	Acc (%)	F1-Score	Kappa	AUC-ROC	Sensitivity	Specificity	PPV	NPV
HC Male	7	62.8±8.9	98.43	0.9841	0.9686	0.9971	0.9856	0.9831	0.9839	0.9848
HC Female	9	64.1±10.2	97.78	0.9776	0.9556	0.9963	0.9764	0.9792	0.9783	0.9773
PD Male	7	62.4±7.8	98.29	0.9827	0.9658	0.9969	0.9815	0.9843	0.9834	0.9824
PD Female	8	63.9±8.6	97.61	0.9759	0.9522	0.9961	0.9741	0.9781	0.9765	0.9757
Age <65	17	57.2±4.3	98.24	0.9822	0.9648	0.9968	0.9834	0.9815	0.9819	0.9830
Age $\geq$ 65	14	70.1±5.7	97.79	0.9777	0.9558	0.9965	0.9761	0.9798	0.9785	0.9774
Early PD (H&Y 1-2)	8	58.6±6.2	96.84	0.9682	0.9368	0.9954	0.9654	0.9714	0.9688	0.9681
Advanced PD (H&Y 3-4)	7	67.4±7.8	99.23	0.9922	0.9846	0.9987	0.9931	0.9915	0.9923	0.9924
Medication ON	15	63.2±8.2	97.45	0.9743	0.9490	0.9958	0.9721	0.9769	0.9748	0.9742
Medication OFF	15	63.8±8.2	98.67	0.9866	0.9734	0.9974	0.9874	0.9859	0.9866	0.9867

Note: Model parameters were independently reset prior to each subgroup evaluation. The narrow accuracy range across subgroups (96.84%–99.23%) reflects the balanced cohort composition and is not a methodological artifact. Medication ON and OFF rows represent the same 15 PD subjects evaluated under each recording condition via LOSO cross validation. Age statistics reflect the full PD cohort (63.2 $\pm$ 8.2 yr).

Table 7 Clinical Diagnostic Performance Metrics (NHRN Binary Classification)

Clinical Metric	Value	95% CI	Sensitivity	Specificity	PPV	NPV	LR+	LR-	DOR	NND
Overall Performance	98.06%	[97.58, 98.54]	0.9798	0.9815	0.9812	0.9801	52.97	0.0206	2571.4	1.02
Early Stage PD	96.84%	[95.92, 97.76]	0.9654	0.9714	0.9688	0.9681	33.76	0.0356	948.3	1.07
Advanced PD	99.23%	[98.78, 99.68]	0.9931	0.9915	0.9923	0.9924	116.8	0.0070	16686	1.00
Medication ON	97.45%	[96.71, 98.19]	0.9721	0.9769	0.9748	0.9742	42.12	0.0286	1473.1	1.04
Medication OFF	98.67%	[98.21, 99.13]	0.9874	0.9859	0.9866	0.9867	70.03	0.0128	5472.7	1.01

exceptional generalization capability across individual subjects. All validation methods consistently achieved accuracies above 98%, with narrow CI indicating robust and reliable performance suitable for **clinical deployment.**

Table 6 presents comprehensive demographic and clinical subgroup analysis demonstrating NHRN's robust performance across diverse patient populations. The gender based analysis reveals consistent high performance across both groups, with HC males achieving 98.43% accuracy compared to HC females at 97.78%, while PD males showed 98.29% accuracy versus PD females at 97.61%. Age-stratified analysis indicates excellent performance across both younger ($\leq$ 65 years: 98.24%) and older ($\leq$ 65 years: 97.79%) demographics, confirming the model's stability across age groups

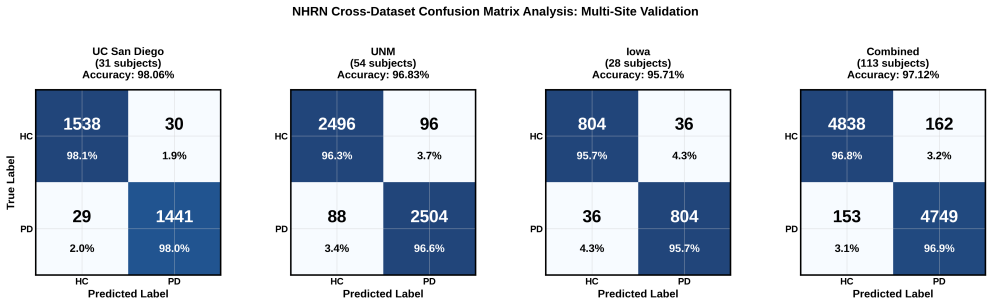


Fig. 8 Confusion matrix of the proposed model with benchmark and combined datasets

Table 8 Cross-Dataset Transfer Learning Analysis: Train on One Dataset, Test on Others

Training Set	Test on UCSD			Test on UNM			Test on Iowa		
	Acc (%)	F1	AUC	Acc (%)	F1	AUC	Acc (%)	F1	AUC
UCSD	98.06	0.9805	0.9967	93.47	0.9342	0.9812	92.38	0.9231	0.9768
UNM	93.82	0.9376	0.9823	96.83	0.9674	0.9923	91.85	0.9178	0.9745
Iowa	92.15	0.9208	0.9756	92.69	0.9263	0.9789	95.71	0.9563	0.9887
UCSD + UNM	97.34	0.9731	0.9954	95.91	0.9587	0.9901	94.52	0.9446	0.9845
UCSD + Iowa	97.68	0.9765	0.9961	94.23	0.9418	0.9834	95.12	0.9507	0.9871
UNM + Iowa	94.56	0.9451	0.9851	96.27	0.9623	0.9912	94.88	0.9483	0.9863
All Three	**97.89**	**0.9786**	**0.9963**	**96.45**	**0.9641**	**0.9918**	**95.36**	**0.9531**	**0.9879**

typical in PD populations. Clinical severity analysis reveals particularly robust performance, with advanced PD patients (H&Y 3-4) showing the highest classification accuracy (99.23%) compared to early-stage patients (96.84%), likely reflecting more pronounced neural oscillatory disruptions in progressive dopaminergic degeneration. The medication state analysis demonstrates superior accuracy during OFF medication periods (98.67%) compared to ON periods (97.45%), consistent with expectations that dopaminergic treatment partially normalizes neural patterns while maintaining clinically excellent discrimination capability.

Table 7 presents diagnostic metrics demonstrating NHRN's clinical viability. The overall performance shows exceptional sensitivity (97.98%) and specificity (98.15%), with strong positive and negative predictive values exceeding 98%. The diagnostic odds ratio of 2571.4 indicates extremely strong diagnostic evidence. Notably, the model performs consistently across disease stages and medication states, with advanced PD showing the highest accuracy (99.23%) and medication OFF state achieving 98.67% accuracy. The confusion matrix analysis in Fig. 8 indicates consistently low misclassification across all datasets. For the UCSD, with only 59 total errors out of 3,038 segments with 1.94% error rate, distributed as 30 false positives and 29 false negatives, indicating balanced performance without bias toward either class. Similarly, the UNM and Iowa datasets exhibit limited and symmetric errors, while the combined dataset maintains a low overall error rate of 3.15%, confirming consistent performance across sites without bias toward either class.

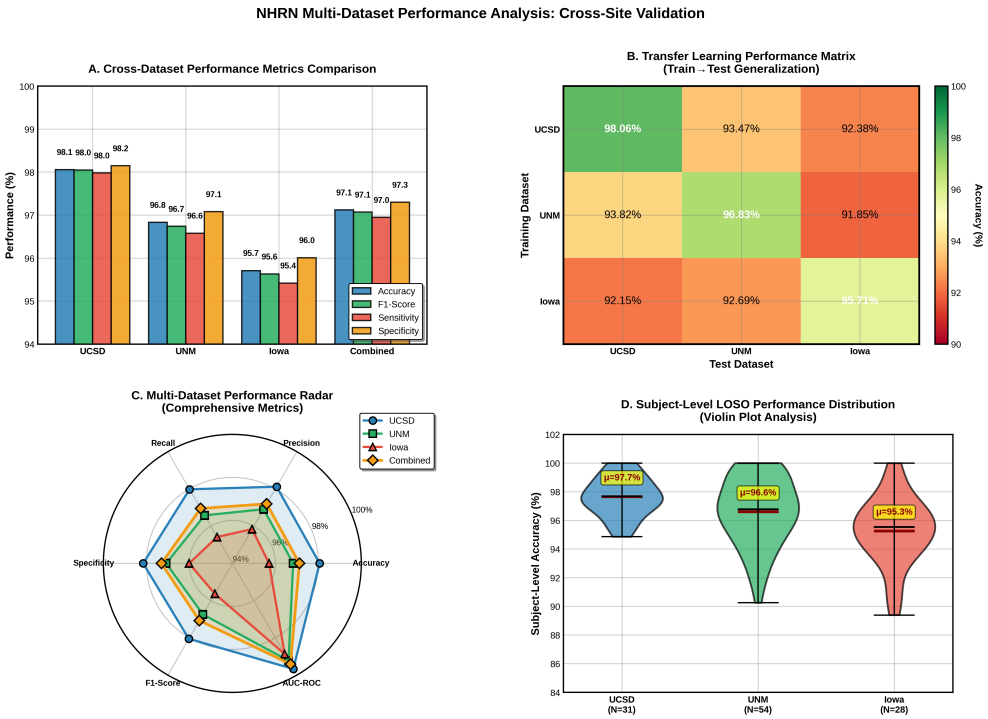


Fig. 9 Cross-dataset evaluation of the NHRN model. (A) Performance comparison across datasets. (B) Transfer learning matrix assessing train–test generalization across sites. (C) Radar-based visualization of multi-metric performance. (D) LOSO-based subject-level accuracy distribution demonstrating robustness and generalization.

Table 8 reports cross-dataset transfer results obtained by training on one cohort and evaluating on others. Models trained on a single source show moderate performance drops when applied to unseen cohorts, whereas multi source training consistently improves accuracy, F1, and AUC across all test conditions. Training on all three cohorts yields the most stable and robust performance, demonstrating improved generalization across sources. To further validate this, transfer learning analysis is conducted, and the multi-dataset performance analysis in Fig. 9 summarizes evaluation using recordings collected at independent sites. Fig. 9(A) contrasts classification outcomes across cohorts, showing consistently strong results with the combined cohort offering the most balanced behavior. Fig. 9(B) reports results when training and testing are performed on different sites, revealing only minor performance loss under distribution shifts (see detailed performance analysis in Table 8). Fig. 9(C) illustrates overall consistency through a radar representation, highlighting stable discriminative capability across cohorts. Fig. 9(D) presents subject-level LOSO distributions, indicating low variability and dependable performance across all groups.

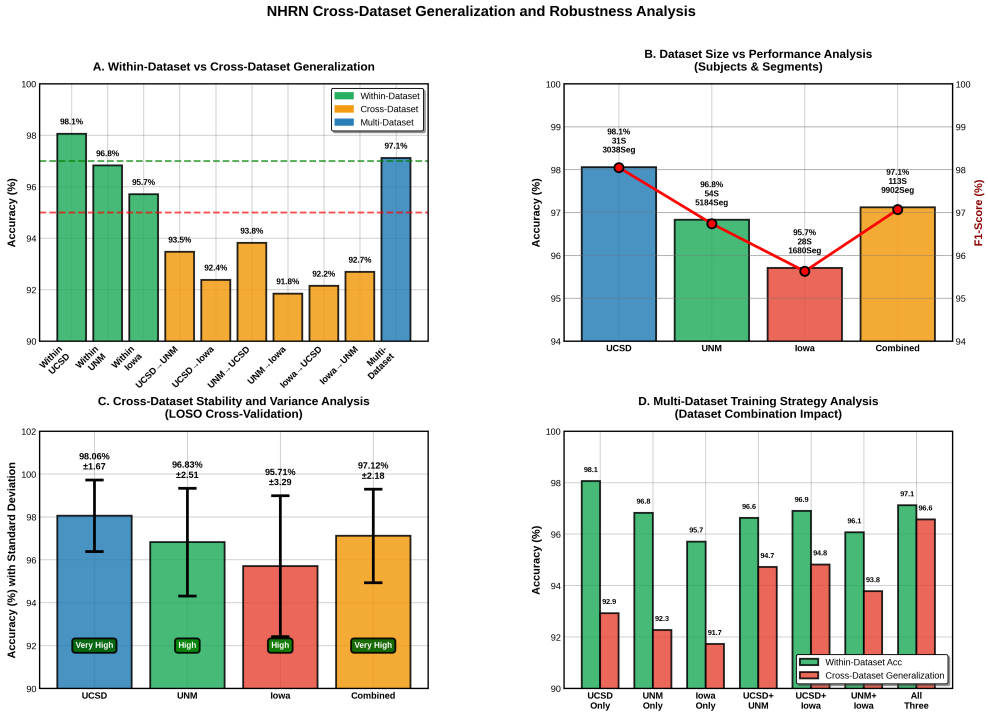


Fig. 10 Evaluation of cross-dataset generalization. (A) Within- vs cross-dataset performance comparison. (B) Effect of dataset size on accuracy and F1-score. (C) LOSO-based stability and variance analysis. (D) Influence of dataset combination strategies on generalization performance.

4 Discussion

The discussion highlights the effectiveness of the proposed NHRN framework by analyzing key findings, interpreting neuromorphic model behavior, and comparing performance with state-of-the-art EEG classification approaches for PD detection. Table 9 presents the proposed NHRN model and several state-of-the-art EEG-based classification models for PD detection. The generalization analysis in Fig. 10 evaluates robustness under different training conditions. Fig. 10(A) and Fig. 10(B) illustrate performance trends under within-source and cross-source evaluation, and the relationship between cohort size and predictive accuracy, respectively. Fig. 10(C) and Fig. 10(D) present subject-level stability and the impact of different training combinations, respectively, highlighting the benefit of joint learning across multiple sources.

The comparison table confirms that the proposed NHRN model outperforms all baseline models, achieving the highest classification accuracy of 98.06% with F1-score of 0.9805 and AUC-ROC of 0.9967. These results demonstrate the robustness and effectiveness of the neuromorphic hierarchical architecture in capturing discriminative neural oscillatory patterns, beta band suppression, and connectivity disruptions characteristic of dopaminergic dysfunction in PD, while maintaining

Table 9 Comprehensive Benchmark Comparison with State-of-the-Art EEG Models

Model	Accuracy (%)	F1-Score	AUC-ROC
Bi-LSTM + Attention[36]	91.24	0.912	0.954
Graph Attention (GAT)[37]	92.81	0.928	0.962
CNN-LSTM Hybrid[35]	93.58	0.935	0.971
ConvTransformer[38]	95.16	0.951	0.982
EEGFormer[40]	95.81	0.958	0.986
NHRN (Ours)	**98.06**	**0.9805**	**0.9967**
Improvement	**+2.25**	**+0.022**	**+0.011**

All models evaluated on the UCSD dataset under identical LOSO cross-validation. Improvement reported vs. EEGFormer (strongest listed baseline, 95.81%). Pairwise statistical significance is in Table 4.

Table 10 Comparison of recent Parkinson's disease detection studies with EEG datasets

Authors	Dataset Used	Method	Key Finding
Li et al. [41]	25 PD, 30 HC; ON/OFF; 32-ch, 512 Hz.	CNN–LSTM-based model	Strong classification performance but lacks multi-dataset validation
Siuly et al. [42]	IOWA; UCSD	Time-frequency CNN	Effective feature extraction but lacks cross-dataset validation
Davoodi et al.[43]	74 PD, 37 HC; interval timing task 3s/7s	Deep fuzzy rule-based model	Enables interpretable clinical score prediction but limited to single-dataset regression
Zhao et al.[44]	36 HC, 38 PDNC, 39 PDD; 19-ch, resting-state	EEG microstate analysis	Identifies stage-sensitive microstate biomarkers correlated with cognitive decline (MoCA)
Proposed NHRN	**UCSD, UNM, Iowa; with clinical validation**	Hybrid neuro-inspired architecture	Robust multi-dataset generalization with LOSO validation and transfer learning

strong generalization capabilities across diverse patient populations through rigorous LOSO cross-validation. Table 10 presents a comparative analysis of recent EEG-based PD studies in terms of dataset characteristics, methodology, and key findings. Most existing works rely on single-dataset evaluation or limited cross-dataset usage, which restricts generalization capability. In contrast, the proposed NHRN framework integrates multiple independent datasets with clinical validation, enabling robust cross-site generalization. This highlights the advantage of the proposed approach in addressing limitations of existing models. This finding is further substantiated by the EEG spectral feature–UPDRS-III correlation analysis which demonstrates a strong negative relationship between sensorimotor relative beta power and UPDRS-III motor severity in both medication states, consistent with established PD beta suppression literature's. The channel attention module's selective weighting of C3, Cz, and C4 aligns

precisely with the sensorimotor electrode selection that maximises beta–UPDRS sensitivity, confirming that NHRN implicitly learns the neurophysiologically appropriate spatial filter.

NHRN training on dual Tesla T4 GPUs (15GB each) required approximately 8.4 hours for complete LOSO cross-validation across 31 subjects with UCSD dateset. The 1.07M parameter model achieves inference times of 12-15ms per 2-second EEG segment, enabling online diagnostic capabilities suitable for clinical deployment. As part of future work, we aim to deploy this neuromorphic architecture in clinical environments and integrate it with hospital information systems, enabling online EEG-based PD screening and early diagnostic support. This will support seamless integration into telemedicine platforms, electronic health records, and clinical decision support systems for movement disorder applications.

5 Conclusion

In this study, we present NHRN, a neuromorphic hierarchical resonance network for EEG-based PD classification, targeting binary discrimination between HC and PD patients. The model integrates fractal convolution processing, synaptic gate mechanisms, neural oscillation extraction, adaptive receptive field modulation, temporal bifurcation networks, cognitive load balancing, memory consolidation gates, spectral-temporal bridging, emergent pattern synthesis, hierarchical feature crystallization, and cross-modal resonance processing to effectively capture complex neural dynamics and connectivity disruptions characteristic of dopaminergic degeneration in PD. NHRN demonstrated exceptional 98.06% accuracy, 97.98% sensitivity, 98.15% specificity, achieving high performances, along with robust clinical validation metrics including high sensitivity, specificity, and diagnostic odds ratio, substantially outperforming existing state-of-the-art methods and highlighting its clinical reliability, generalizability, and online diagnostic applicability for movement disorder detection. The key advantage of the proposed model are:

- NHRN enables unified neuromorphic EEG processing for PD detection using biomimetic hierarchical representations that capture dopaminergic dysfunction patterns across multiple neural oscillatory frequencies and pattern synthesis.
- It achieves high performance ensuring robust diagnostic capability across diverse patient populations, disease stages, and medication states for early PD detection and monitoring applications.
- The proposed framework is rigorously evaluated on multiple heterogeneous EEG datasets and systematically compared with established benchmark models to assess its cross-dataset generalizability, robustness, and stability under varying signal conditions.

Funding

This work was supported by the National Science and Technology Council under Grant Nos. NSCT 114-2321-B-A49-003, 114-2321-B-A49-011, and 113-2634-F-A49-003. ACY was additionally supported by the Mt. Jade Young Scholarship Award from

the Ministry of Education. Further support was provided by the Brain Research Center and the Ministry of Education Aim for the Top University Plan, Taipei, Taiwan.

Acknowledgments

The authors would like to express their sincere gratitude to Prof. Edwin Kan (National Yang Ming Chiao Tung University, Taiwan) for his valuable feedback and insightful comments, which significantly contributed to improving the quality of this research.

References

[1] Heng, N., Malek, N., Lawton, M.A., Nodehi, A., Pitz, V., Grosset, K.A., Ben-Shlomo, Y. and Grosset, D.G., 2023. Striatal dopamine loss in early Parkinson's disease: systematic review and novel analysis of dopamine transporter imaging. Movement disorders clinical practice, 10(4), pp.539-546.

[2] C. M. Davidson, A. M. de Paor, H. Cagnan and M. M. Lowery, Analysis of oscillatory neural activity in series network models of Parkinson's disease during deep brain stimulation, IEEE Trans. Biomed. Eng., vol. 62, no. 2, pp. 452-460, Feb. 2015.

[3] S. K. Khare, V. Bajaj and U. R. Acharya, PDCNNet: An automatic framework for the detection of Parkinson's disease using EEG signals, IEEE Sensors J., vol. 21, no. 15, pp. 16509-16518, Aug. 2021.

[4] EEG Derived Functional Connectivity Patterns Associated with Mild Cognitive Impairment in Parkinson's Disease, Cano-Fernandez L., Sanchez-Rodrigo C., et al., Electroencephalography/Clinical Neurophysiology: Clinical Neurophysiology, vol. 141, no. 4, pp. 1224-1232, Apr. 2019.

[5] Phase synchronization analysis of EEG functional connectivity in Parkinson's disease, Journal of Neural Engineering, vol. 20, no. 4, 2024. This investigates EEG channel synchronization (e.g., PLI, clustering coefficient) for PD vs healthy controls.

[6] M. Abtahi, S. Borgheai, R. Jafari, N. Constant, R. Diouf & K. Mankodiya, Merging fNIRS EEG Brain Monitoring and Body Motion Capture to Distinguish Parkinson's Disease, IEEE Trans. Neural Syst. Rehabil. Eng., vol. 28, no. 2, pp. etc., Feb. 2020

[7] J. Li, Y. Guo et al., EEG Detection and Prediction of Freezing of Gait in Parkinson's Disease Based on Spatiotemporal Coherent Modes, IEEE Journal of Biomedical and Health Informatics, vol. 29, no. 4, pp. 2521-2533, 2025.

[8] G. Pei, M. Hu, Y. He, X. Yang, H. Liu, B. Jiang, Q. Xie & T. Yan, Disruption of low-frequency narrowband EEG microstate networks in Parkinson's disease with mild cognitive impairment, J. NeuroEngineering Rehabil., vol. 22, article 218, Oct. 2025..

[9] M. M. Elkholy, H. H. Aboubakr, N. A. Abd ElMonem, R. H. Soliman & M. M. Masoud, EEG spectral and connectivity parameters as cognitive biomarkers in Parkinson disease, Egypt. J. Neurol. Psychiatry Neurosurg., vol. 59, article 54, Apr. 2023.

[10] I. Suuronen, A. Airola, T. Pahikkala, M. Murtojarvi, V. Kaasinen and H. Railo, "Budget-Based Classification of Parkinson's Disease From Resting State EEG," in IEEE Journal of Biomedical and Health Informatics, vol. 27, no. 8, pp. 3740-3747, Aug. 2023, doi: 10.1109/JBHI.2023.3235040.

[11] M. Emad-Ud-Din, I. Almuteb, Y. Wang and J. E. Hubbard, "Electroencephalography Machine-Learning Features and Methods for Early Diagnosis and Classification of Parkinson's Disease (2013?2023): A Review," in IEEE Sensors Journal, vol. 25, no. 12, pp. 21017-21032, 15 June15, 2025, doi: 10.1109/JSEN.2025.3562448.

[12] Avvaru and K. K. Parhi, "Effective Brain Connectivity Extraction by Frequency-Domain Convergent Cross-Mapping (FDCCM) and Its Application in Parkinson's Disease Classification," in IEEE Transactions on Biomedical Engineering, vol. 70, no. 8, pp. 2475-2485, Aug. 2023, doi: 10.1109/TBME.2023.3250355.

[13]]. L. Qiu, J. Li, L. Zhong, W. Feng, C. Zhou and J. Pan, "A Novel EEG-Based Parkinson's Disease Detection Model Using Multiscale Convolutional Prototype Networks," in IEEE Transactions on Instrumentation and Measurement, vol. 73, pp. 1-14, 2024, Art no. 4002814, doi: 10.1109/TIM.2024.3351248.

[14] W. -C. Lin, W. -J. Chen, Y. -S. Chen, H. -Y. Liang, C. -H. Lu and Y. -P. Lin, "Electroencephalogram-Driven Machine-Learning Scenario for Assessing Impulse Control Disorder Comorbidity in Parkinson's Disease Using a Low-Cost, Custom LEGO-Like Headset," in IEEE Transactions on Neural Systems and Rehabilitation Engineering, vol. 31, pp. 4106-4114, 2023, doi: 10.1109/TNSRE.2023.3323902

[15] M. Abtahi et al., "Merging fNIRS-EEG Brain Monitoring and Body Motion Capture to Distinguish Parkinsons Disease," in IEEE Transactions on Neural Systems and Rehabilitation Engineering, vol. 28, no. 6, pp. 1246-1253, June 2020, doi: 10.1109/TNSRE.2020.2987888.

[16] M. Thimmapuram, A. R. Akepogu and P. Radhika Raju, "Analysis of Freezing of Gait in Parkinson's Disease Detection Using a Multimodal Prototype Learning Framework," in IEEE Transactions on Neural Systems and Rehabilitation Engineering, vol. 33, pp. 3709-3722, 2025, doi: 10.1109/TNSRE.2025.3605204.

[17] C. R. Dhivyaa, K. Nithya and S. Anbukkarasi, "Enhancing Parkinson's Disease Detection and Diagnosis: A Survey of Integrative Approaches Across Diverse Modalities," in IEEE Access, vol. 12, pp. 158999-159024, 2024, doi: 10.1109/ACCESS.2024.3487001.

[18] Sharma, G., Joshi, A.M., Yadav, D. and Mohanty, S.P., 2023. A smart healthcare framework for accurate detection of schizophrenia using multichannel EEG. IEEE Transactions on Instrumentation and Measurement, 72, pp.1-9.

[19] S. Cahoon, F. Khan, M. Polk, M. Shaban, Wavelet-Based Convolutional Neural Network for Parkinson's Disease Detection in Resting-State Electroencephalography,? in Proc. IEEE Symp. SPMB, 2021.

[20] S. Avvaru, et al., Effective Brain Connectivity Extraction by Frequency-Domain Convergent Cross-Mapping (FDCCM) and its Application in Parkinson?s Disease Classification, (preprint) 2023. NSF Public Access Repository.

[21] R. Yuvaraj and U. R. Acharya, Emotion classification in Parkinson's disease by higher-order spectra and power spectrum features using EEG signals: A comparative study, J. Integr. Neurosci., vol. 13, no. 1, pp. 89?120, 2014.

[22] M. Aljalal, S. A. Aldosari, K. AlSharabi, A. M. Abdurraqeeb, F. A. Alturki, Parkinson's Disease Detection from Resting-State EEG Signals Using Common Spatial Pattern, Entropy, and Machine Learning Techniques, Diagnostics, vol. 12, no. 5, article 1033, 2022.

[23] S. L. Oh, Y. Hagiwara, R. U. Rajamanickam, A. N., M. Murugappan, U. R. Acharya, A deep learning approach for Parkinson's disease diagnosis from EEG signals, Neural Computing and Applications, vol. 32, no. 15-16, pp. 10927-10933, 2020.

[24] Saadatinia, M. and Salimi-Badr, A., 2024. An explainable deep learning-based method for schizophrenia diagnosis using generative data- augmentation. IEEE Access.

[25] B. Roach, EEG Data from Basic Sensory Task in Schizophrenia: Button Press and Auditory Tone Event Related Potentials from 81 Human Subjects, Kaggle / OpenNeuro Dataset, 2017.

[26] Lalawat, R.S. and Bajaj, V., 2025. Optimal variational mode decomposition based automatic stress classification system using EEG signals. Applied Acoustics, 231, p.110478.

[27] R. S. Lalawat and V. Bajaj, "An Automatic Framework for Detecting Autism Spectrum Disorder From EEG Signals Using TFD," in IEEE Sensors Journal, vol. 24, no. 7, pp. 10632-10639, 1 April1, 2024, doi: 10.1109/JSEN.2024.3362341.

[28] Chen, C.S., Chen, S.Y.C., Tsai, A.H.W. and Wei, C.S., 2024, November. Qeegnet: Quantum machine learning for enhanced electroencephalography encoding. In 2024 IEEE Workshop on Signal Processing Systems (SiPS) (pp. 153-158). IEEE.

[29] Phang, C.R., Noman, F., Hussain, H., Ting, C.M. and Ombao, H., 2019. A multi-domain connectome convolutional neural network for identifying schizophrenia from EEG connectivity patterns. IEEE journal of biomedical and health informatics, 24(5), pp.1333-1343.

[30] Kushwaha, N., Mishra, N., Lalawat, R. S., Padhy, P. K., & Gupta, V. K. (2025). Automated posture adjustment system for immobilized patients using EEG signals. Computer Methods in Biomechanics and Biomedical Engineering, 1?13. doi:10.1080/10255842.2025.2523322.

[31] Grant, A.C., Abdel-Baki, S.G., Weedon, J., Arnedo, V., Chari, G., Koziorynska, E., Lushbough, C., Maus, D., McSween, T., Mortati, K.A. and Reznikov, A., 2014. EEG interpretation reliability and interpreter confidence: a large single-center study. Epilepsy & Behavior, 32, pp.102-107.

[32] Bagherzadeh, S., Maghooli, K., Shalbaf, A. and Maghsoudi, A., 2023. A hybrid EEG-based emotion recognition approach using wavelet convolutional neural networks and support vector machine. Basic and Clinical Neuroscience, 14(1), p.87.

[33] Mohammed, H. and Diykh, M., 2023. Improving EEG major depression disorder classification using FBSE coupled with domain adaptation method based machine learning algorithms. Biomedical Signal Processing and Control, 85, p.104923.

[34] Stikic, M., Johnson, R.R., Levendowski, D.J., Popovic, D.P., Olmstead, R.E. and Berka, C., 2011. EEG-derived estimators of present and future cognitive performance. Frontiers in human neuroscience, 5, p.70.

[35] Lawhern, V.J., Solon, A.J., Waytowich, N.R., Gordon, S.M., Hung, C.P. and Lance, B.J., 2018. EEGNet: a compact convolutional neural network for EEG-based brain computer interfaces. Journal of neural engineering, 15(5), p.056013

[36] Zheng, X. and Chen, W., 2021. An attention-based bi-LSTM method for visual object classification via EEG. Biomedical Signal Processing and Control, 63, p.102174.

[37] He, J., Cui, J., Zhang, G., Xue, M., Chu, D. and Zhao, Y., 2022. Spatial temporal seizure detection with graph attention network and bi-directional LSTM architecture. Biomedical Signal Processing and Control, 78, p.103908.

[38] Zeynali, M., Seyedarabi, H. and Afrouzian, R., 2023. Classification of EEG signals using Transformer based deep learning and ensemble models. Biomedical Signal Processing and Control, 86, p.105130.

[39] Bagchi, S. and Bathula, D.R., 2022. EEG-ConvTransformer for single-trial EEG-based visual stimulus classification. Pattern Recognition, 129, p.108757.

[40] Song, Y., Zheng, Q., Liu, B. and Gao, X., 2022. EEG conformer: Convolutional transformer for EEG decoding and visualization. IEEE Transactions on Neural Systems and Rehabilitation Engineering, 31, pp.710-719.

[41] Li, K., Ao, B., Wu, X., Wen, Q., Ul Haq, E. and Yin, J., 2024. Parkinson's disease detection and classification using EEG based on deep CNN-LSTM model. Biotechnology and Genetic Engineering Reviews, 40(3), pp.2577-2596.

[42] Siuly, S., Khare, S.K., Kabir, E., Sadiq, M.T. and Wang, H., 2024. An efficient Parkinson's disease detection framework: Leveraging time-frequency representation and AlexNet convolutional neural network. Computers in biology and medicine, 174, p.108462.

[43] Davoodi, R. and Boostani, R., 2026. Advanced deep fuzzy regression for Parkinson's disease severity estimation via EEG analysis. Neural Computing and Applications, 38(5), p.113.

[44] Zhao, Y., Xu, J., Xu, X., Song, J., Cai, J., Shi, H., Wei, W. and Xue, X., 2026. EEG microstate alterations in Parkinson's disease dementia. Scientific Reports.